J. Fluid Mech. (1992), *vol.* 245, *pp.* 69–90

Investigation of a co-flowing buoyant jet: experiments on the effect of Reynolds number and Richardson number

By E. R. SUBBARAO† AND B. J. CANTWELL

Department of Aeronautics and Astronautics, Stanford University, Stanford, CA 94305, USA

(Received 12 April 1990 and in revised form 9 August 1991)

Experiments have been carried out on a vertical jet of helium issuing into a co-flow of air at a fixed exit velocity ratio of 2.0. At all the experimental conditions studied, the flow exhibits a strong self-excited periodicity. The natural frequency behaviour of the jet, the underlying flow structure, and the transition to turbulence have been studied over a wide range of flow conditions. The experiments were conducted in a variable-pressure facility which made it possible to vary the Reynolds number and Richardson number independently. A stroboscopic schlieren system was used for flow visualization and single-component laser-Doppler anemometry was used to measure the axial component of velocity. The flow exhibits several interesting features. The presence of co-flow eliminates the random meandering typical of buoyant plumes in a quiescent environment. The periodicity of the helium jet under high-Richardson-number conditions is striking. Under these conditions transition to turbulence consists of a rapid but highly structured and repeatable breakdown and intermingling of jet and free-stream fluid. At $Ri = 1.6$ the three-dimensional structure of the flow is seen to repeat from cycle to cycle. The point of transition moves closer to the jet exit as either the Reynolds number or the Richardson number increases. The wavelength of the longitudinal instability increases with Richardson number. At low Richardson numbers, the natural frequency scales on an inertial timescale, $\tau_1 = D/U_j$ where D is the jet diameter and U_j is the mean jet exit velocity. At high Richardson number, the natural frequency scales on a buoyancy timescale, $\tau_2 = [\rho_j D/g(\rho_\infty - \rho_j)]^{\frac{1}{2}}$ where g is the gravitational acceleration and ρ_j and ρ_∞ are the jet and free-stream densities respectively. The transition from one flow regime to another occurs over a narrow range of Richardson numbers from 0.7 to 1. A buoyancy Strouhal number is used to correlate the high-Richardson-number frequency behaviour.

1. Introduction

Buoyancy-dominated jets are common in an industrialized environment. Cooling water discharging into a lake, high-temperature gas issuing from a stack, the discharge of a cooling tower, or a low-speed flame are typical examples. To our knowledge the case of a buoyant jet in the presence of co-flow has not been studied previously. The co-flow has the effect of eliminating the random meandering associated with buoyant plumes with zero external velocity, leading to a flow which exhibits an unusual degree of regularity.

The goal of the research was to study the behaviour of the jet over a wide range

† Present Address: Hughes Aircraft Company. PO Box 92919, Los Angeles, CA 90009-2919, USA.

of governing parameters with emphasis on flow structure and the scaling properties of the natural frequency of the jet. The work was motivated partly by recent experiments by Strawa & Cantwell (1989) in low-speed diffusion flames subject to a classical flickering instability. A number of investigators have studied the natural-frequency behaviour of jet diffusion flames. Chamberlin & Rose (1928), and Kimura (1965) studied jet diffusion flames with and without co-flow; Grant & Jones (1975), and Ballantyne & Bray (1977) studied free-jet diffusion flames. They have all reported a natural flickering instability between 9 and 15 Hz. At the low jet velocities reported, it would appear that the appropriate non-dimensionalizing parameter for the flickering frequency would be the buoyancy timescale; the typical time for fluid exiting the jet to move one jet diameter under the acceleration of gravity. However, Chamberlin & Rose found that the fuel type, jet exit velocity, and jet diameter did not appear to strongly affect the flicker frequency and attempts to correlate frequency data from low-speed jet flames have not met with much success (Becker & Liang 1983). The phenomenon is dominated by, but not solely dependent upon, buoyancy. In contrast, recent studies of the formation of organized structures in pool fires by Zukoski, Cetegen & Kubota (1984) and Schonbucher *et al.* (1986) indicate that the natural frequency in this case does scale with the buoyancy timescale of the flow over a wide range of fire diameters.

From a study of this work it appears that one might understand the scaling properties of flickering flames by distinguishing various cases on the basis of how buoyancy is released near the jet exit. At one limit is the diffusion flame where the buoyancy is released in a relatively thin cylindrical sheet. The complex interplay between the jet exit velocity field, the position of the flame sheet and the stability of the plume which rises from the point of ignition makes the downstream development of the flame extremely sensitive to perturbations of the jet exit flow.

At the other limit is the helium jet where the buoyancy is released more-or-less uniformly across the entire jet cross-section. The complicating effects of chemical reactions and the associated local instabilities of the flame sheet are removed while retaining approximately the same density ratio of hot combustion products to air. The pool fire may lie somewhere in between. Although there are sharp gradients of density and velocity above the surface of the pool, the low velocities, rapid mixing and high heat transfer rates in this region suggest that the release of buoyancy is not confined to a plume surrounding the edges of the pool but is distributed across the pool surface and this may account for the dependence of the natural frequency on the buoyancy timescale in this case.

There are virtually no data in the literature on buoyant jets with co-flow although this geometry is commonly used in the study of flames. Most of the data which do exist are for weakly buoyant plumes in water. Fay (1973) reviews work on buoyant plumes and buoyant vehicular wakes and provides scaling laws for the asymptotic form of plume rise. A recent comprehensive article by Gebhart, Hilder & Kelleher (1984) reviews theoretical models, experimental data, and computer models of both planar and axisymmetric buoyant jets. We also make reference here to the work of Chen & Rodi (1980) who have critically evaluated experimental data on vertical turbulent buoyant jets in uniform media.

Relatively little is known about the strongly buoyant case with Richardson numbers above 0.5 except that derived from fire studies, and virtually nothing is known about the effects of co-flow. As a consequence basic questions about flow structure, stability and transition to turbulence need to be answered. Simple scaling properties of the flow are of interest and in the course of this work a buoyancy

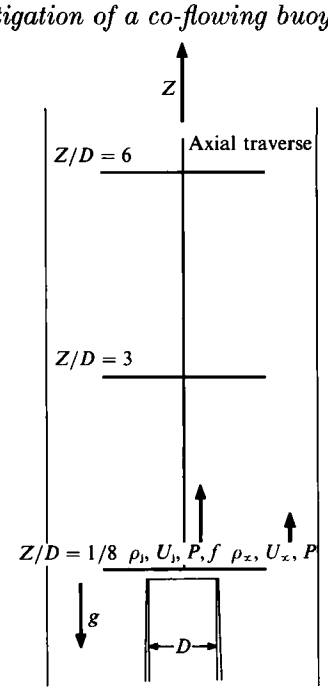

FIGURE 1. Schematic showing flow configuration, relevant parameters, and velocity measurement stations.

Strouhal number was defined and used to correlate frequency data from the approximately seventy different Reynolds number and Richardson number cases studied. The buoyancy Strouhal number was found to be nearly independent of Reynolds number and Richardson number for Richardson numbers larger than one.

2. Flow configuration and experimental parameters

Figure 1 shows a schematic of the flow geometry. The jet diameter was 2.54 cm. The jet exit flow was laminar (parabolic profile) and the average exit velocity ranged from approximately 0.5 m/s to approximately 5 m/s. The test section pressure ranged from 2 to 5 atmospheres.

The relevant dimensionless numbers are the Reynolds number, Re, the Richardson number, Ri, the Strouhal number, St, and the ratio of the velocities of the jet and free stream, U_j/U_∞. We will use a Reynolds number based on jet exit mean velocity and jet fluid properties. The Richardson number, which is a measure of the relative strengths of inertial and buoyancy forces, can be written as

$$Ri = \frac{gD}{U_j^2}\frac{(1-\rho_j/\rho_\infty)}{\rho_j/\rho_\infty}. \tag{1}$$

The flow is inertially dominated for Richardson numbers significantly less than unity, and buoyancy dominated if the Richardson number is significantly greater than unity. For a given geometry and gas composition the Reynolds number and Richardson number can be shown to depend only on the jet exit velocity and test section pressure. The Reynolds number is proportional to the product of test section pressure and velocity. For the present experiment

$$Re = 199.84\left(\frac{P}{P_{atm}}U_j\right). \tag{2}$$

The Richardson number is proportional to the inverse square of the jet exit velocity. For the conditions of this experiment

$$Ri = 1.504/U_j^2, \tag{3}$$

where U_j is the average jet exit velocity in m/s and P is the test section pressure.

By controlling the jet and free-stream velocities and test section pressure the Reynolds number and Richardson number were varied independently at a fixed velocity ratio $U_j/U_\infty = 2.0$.

3. Experimental apparatus

The flow facility draws its airflow from a large sphere at high pressure. The test section, turbulence suppression section and associated plumbing are designed for elevated pressures up to a maximum of 10 atmospheres. The mass flow rate through the system and the test section pressure are controlled by upstream and downstream control valves. Both valves operate in the choked condition (pressure ratio > 2) and the flow exhausts through a fume hood to the atmosphere. Details concerning the facility may be found in Strawa (1986).

Figure 2 shows a cutaway view of the flow facility and the jet model. The turbulence suppression section contains perforated plates, honeycomb, screens, an axisymmetric contraction, and a circular to rectangular transitional contraction. The test section is 10 by 15 cm in cross-section and is approximately 48 cm long. Four windows provide optical access for LDA measurements and schlieren visualization. Checks on flow uniformity and free-stream turbulence level were made for a wide range of pressures and velocities, and the free-stream turbulence intensity is under 1 % over the range of velocities used. Complete tabulation of the flow quality studies and experimental results may be found in Subbarao (1987).

The flow system for the jet is shown in figure 2 and consists of a diffuser with screens, a straight section with honeycomb, a contraction and a straight 2.54 cm diameter jet tube 45 diameters long. The last 6 diameters are tapered on the outside of the pipe to reduce the wall thickness to 0.083 cm at the jet lip. Exit velocity profile data are shown in figure 3 for a wide range of exit flow Reynolds numbers. As one would expect, the exit flow profile is very close to the parabolic shape of a fully developed pipe flow profile. Small deviations from the parabolic shape apparent in the figure are due to fluctuations in the exit velocity induced by unsteady vortex formation just downstream of the exit (which flattens the mean profile slightly) and by acceleration of the exit flow due to buoyancy and the co-flow which causes the exit velocity to slightly exceed the velocity expected for a fully developed pipe flow. Conditional measurements of the exit velocity profile as a function of the phase of the vortex formation process can be found in Subbarao (1987). Checks on axisymmetry of the mean flow at the jet exit were made and appear in figure 3, which includes measurements in two orthogonal diametric planes. The exit flow is well-defined and repeatable.

A stroboscopic schlieren system set up in a standard 'Z' configuration was used to visualize the flow. The slit and knife edge were both horizontal to reveal density gradients in the vertical direction. The stroboscopic system provided a very effective means of determining the natural frequency of the flow and made it possible to take short-exposure photographs. Initial studies involved the use of schlieren photography to document the flow structure. Multiple-exposure photographs at a given phase were also taken to identify aspects of the flow structure which were repeatable

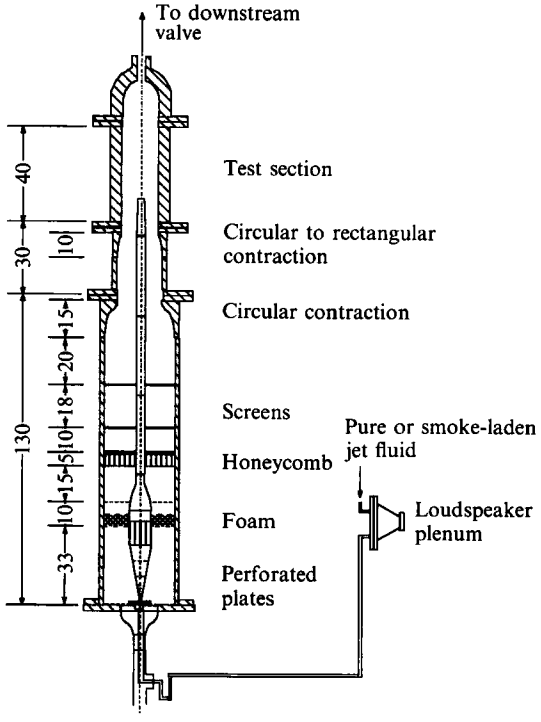

FIGURE 2. Cutaway view of model and flow facility. All dimensions are in cm.

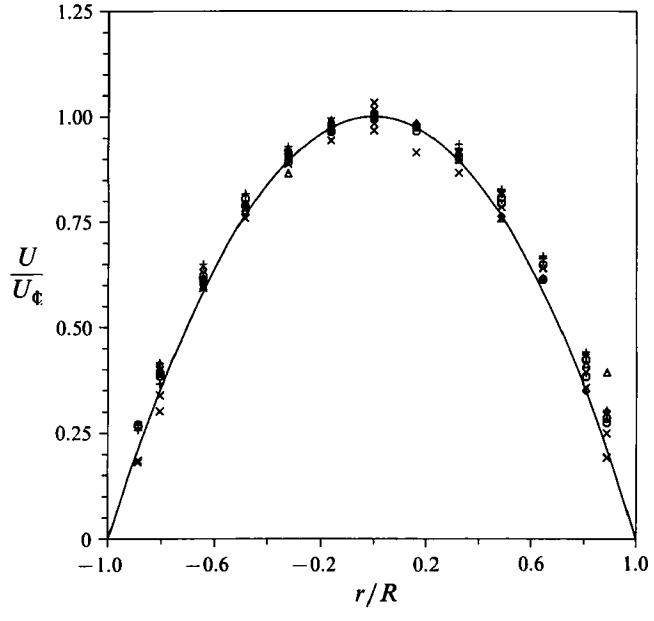

FIGURE 3. Mean velocity profile near the jet exit ($Z/D = \frac{1}{8}$): +, air, $Re = 2150$; ⏀, air, $Re = 1275$; △, air, $Re = 830$; ×, He, $Re = 390$; ◇, He, $Re = 195$; ——, parabolic profile.

over many cycles. To address issues of flow repeatability, as well as to aid in studying flow dynamics, 16 mm high-speed movies were made using a continuous light source for the schlieren system. Early flow visualization studies revealed that, under most conditions, the flow exhibits a strong natural periodicity in the form of a longitudinal

Case	U_j (m/s)	U_∞ (m/s)	P (psia)	f (Hz)	Re	Ri	St
A	0.55	0.28	53	16.4	390	4.97	0.76
B	0.96	0.48	30.5	23.3	390	1.63	0.62
C	0.97	0.47	61	23.8	790	1.6	0.62
D	1.61	0.79	36	28.3	772	0.58	0.45

TABLE 1. Summary of flow cases selected for detailed velocity measurements

instability. To provide a synchronization pulse for phase-conditioned data acquisition, the jet was excited by adding a perturbation to the jet exit velocity. Photographs were taken of the unexcited jet, of a strongly driven jet and of the weakly excited jet driven at a low level sufficient to synchronize the flow with the external clock of the data collection system. In the latter case the amplitude of the excitation was small enough so that there was no visual difference between the self-excited flow and the driven flow. Velocity measurements confirm that the velocity fluctuations at the jet exit were the same for the self-excited and the weakly driven cases (Subbarao 1987). Strong excitation has relatively little effect on flow structure unless the imposed perturbations are very large. The results described here will be restricted to the weakly excited case. The excitation chamber, shown in figure 2, is approximately 20.3 cm in diameter and 10.15 cm deep and contains a loudspeaker which is used as a volume source to provide a periodic variation in flow velocity at the jet exit.

The flow was explored at various Reynolds numbers and Richardson numbers and selected cases were identified for detailed velocity measurements. The velocity data consist of profiles of the streamwise component measured at positions indicated in figure 1. Cross-stream profiles for the excited and unexcited cases were measured on two orthogonal diameters close to the jet exit ($Z/D = \frac{1}{8}$) to document initial conditions and exit flow symmetry. Cross-stream profiles at $Z/D = 3$, and $Z/D = 6$ were also measured. A traverse at eight positions along the jet centreline from $Z/D = \frac{1}{8}$ to $\frac{13}{2}$ was made to document the axial decay due to mixing. In all cases data were collected with the inner (jet) flow and outer (free-stream) flow seeded separately. With the inner flow seeded, the presence of seed denoted the boundary of the jet (as distinct from the boundary of the helium which diffuses into the surrounding air). With the outer flow seeded, seed particles were found within the jet boundaries due to mixing and engulfment of air. Outer fluid was first found to penetrate to the jet centreline approximately two diameters downstream of the jet exit. The range of parameters for the visualization was

$$0.12 \leqslant Ri \leqslant 7.4, \quad 200 \leqslant Re \leqslant 1640, \tag{4}$$

where the Reynolds number is based on the mean jet exit velocity and helium kinematic viscosity. Table 1 presents the flow conditions and associated velocity, pressure, and natural frequency values for the cases selected for detailed velocity measurement.

A laser-Doppler anemometer (LDA) system in forward scatter utilizing the green 514.5 nm line of an Argon ion laser was used to make the velocity measurements. Mineral oil smoke was used for the LDA seeding. The laser and optical components were fixed rigidly to a three-dimensional traversing table, enabling alignment of the optics to be maintained at all times. Focal volume position was measured by two dial indicators that referenced the sides of the test section, and by a height gauge that

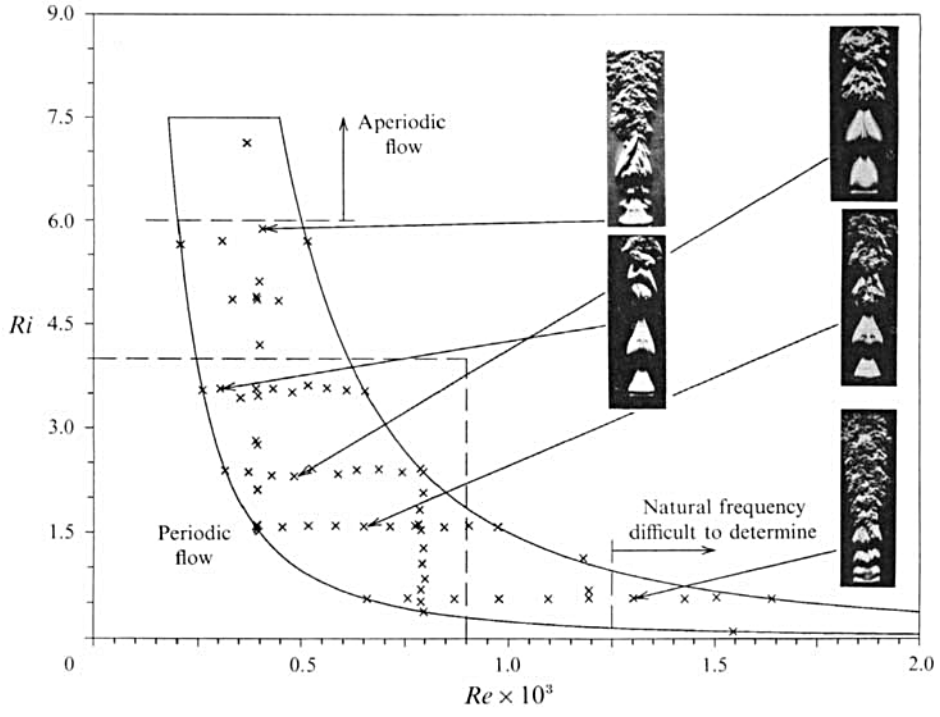

FIGURE 4. Map of flow facility operating range in Re-Ri space. Photos depict typical flow states. Dashed line encloses region of periodic flow.

referenced a fixed mark on the test section. The phase of a primary clock for the flow excitation system was recorded along with the LDA data and used later to sort the data into bins at 30° increments in the phase.

4. Results and discussion

4.1. *Flow structure*

The effect of pressure on the operating envelope of the experiments can be seen by eliminating velocity from (2) and (3) to give

$$Re = 245(P/P_{\text{atm}})/Ri_{\frac{1}{2}}^{\frac{1}{2}}. \tag{5}$$

Figure 4 shows the limits of operation in Reynolds number–Richardson number coordinates and indicates with a cross each of the seventy-four experimental conditions studied. A few representative photographs are included to indicate some of the flow states that are possible. The comments on this figure briefly indicate the behaviour of the flow in different regimes. At very high Richardson numbers (low jet exit velocity) the flow is aperiodic and follows a meandering, irregular course typical of strongly buoyant flows in the absence of co-flow. At moderate values of Richardson number greater than one an extremely regular flow state is found consisting of the periodic formation and breakdown of helium-containing vortical cells. The post-breakdown form of these cells is unusual in that the three-dimensional structure of the flow is extremely repeatable from cycle to cycle and over thousands of cycles of the basic longitudinal instability. At low values of the Richardson number the natural frequency of the jet increases, tending to approach the non-buoyant case.

The schlieren photographs in figure 5 show the flow structure observed at various

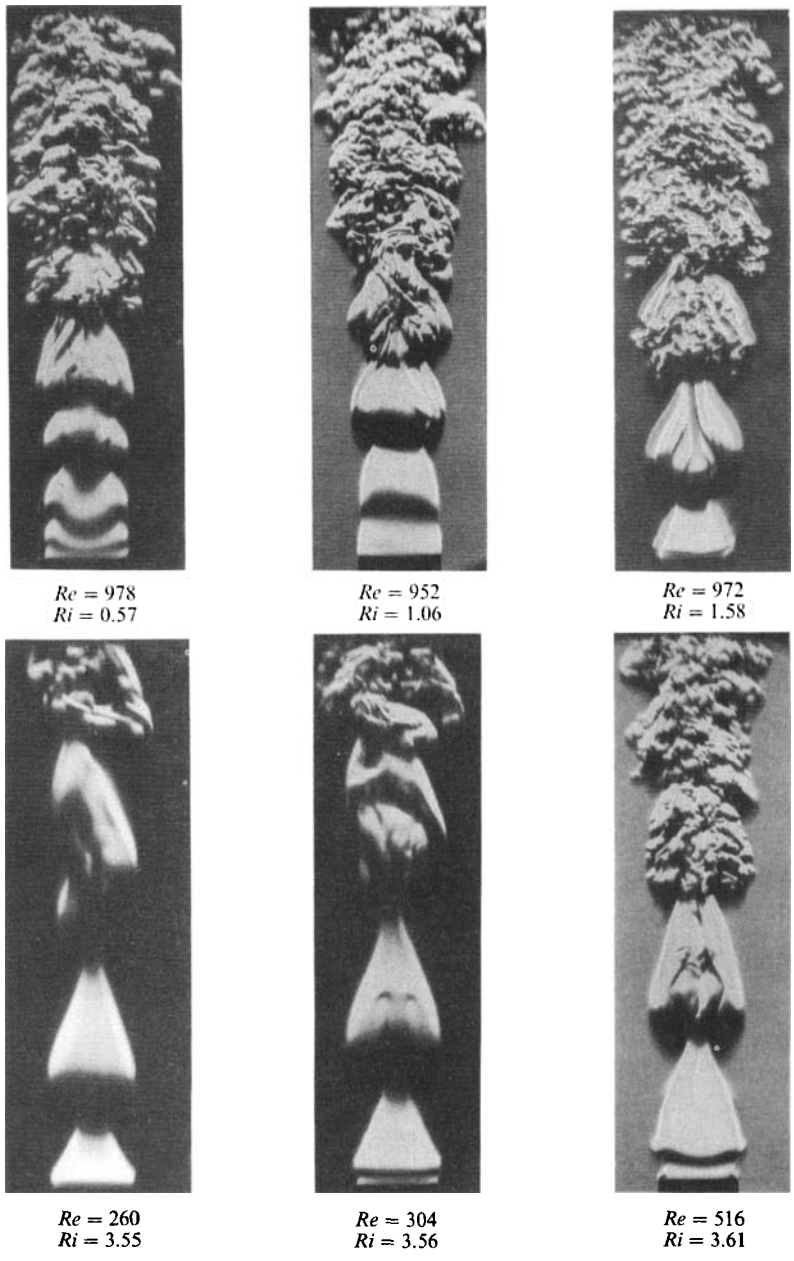

FIGURE 5. The effect of Richardson number and Reynolds number on transition to turbulence and cell wavelength.

Reynolds numbers and Richardson numbers. In the upper set of three photographs the Richardson number is varied by a factor of about three while the Reynolds number is held approximately constant. The most obvious change is the increase in the wavelength of the basic instability of the jet as the Richardson number increases. Buoyancy causes fluid on the centreline of the jet to be accelerated. If one considers the effect of buoyancy on the vortical cells, the centre of the cell is accelerated while the periphery moves at a speed intermediate between the centreline and free-stream velocity. This suggests that higher Richardson numbers will give rise to more-

stretched cells or to longer wavelengths. In the lower set of photographs in figure 5, the Reynolds number varies by a factor of two at a fixed, high, Richardson number. In this case the wavelength is almost fixed, indicating the inviscid, buoyancy-dependent character of the basic instability. It should be noted that, although the core fluid is strongly accelerated at high Richardson number, the envelope of the cells which defines the wavelength of the flow structure tends to move at a nearly constant speed. This was also noted in the case of the flame studied by Strawa & Cantwell (1989, figures 5, 6 and 7).

Transition to turbulence in all the cases depicted in figure 5 is sudden and appears to occur without a gradual change of scale. The effect of increasing Reynolds number is to cause the transition point to approach the jet exit, as would be expected. The effect of increasing Richardson number is also to cause the transition point to approach the jet exit. In the upper sequence of photos, at fixed Reynolds number, the increase of Richardson number from left to right can be thought of as equivalent to increasing the Grashof number ($Gr = Ri \times Re^2$). For a given kinematic viscosity and jet exit velocity, increasing Grashof number will lead to a higher rate of acceleration of the jet fluid giving rise to faster core velocities, locally higher Reynolds numbers, and a more unstable flow. The greater the buoyancy, the greater the acceleration and therefore the closer to the jet exit transition ought to occur. However, this effect does not increase without limit as the Grashof number increases. For a choice of fluid density ratio, there is a limit to the maximum acceleration of an element of buoyant fluid. This limit is imposed by viscous drag and by the resistance associated with the apparent mass of the accelerating fluid. The velocity data from this experiment and from the flame studies of Strawa & Cantwell (1988) indicate that acceleration rates as high as $3g$ can occur, suggesting that buoyant parcels of fluid assume a relatively elongated streamlined shape as they rise. However, the acceleration rates clearly are limited and one would expect that at high velocities such streamlined blobs of helium would tend to become unstable and break up into shorter segments with lower acceleration rates. It is therefore reasonable to expect an asymptotic value for both transition distance and wavelength as the Richardson number increases.

At Richardson numbers above unity the three-dimensional breakdown to turbulence occurs suddenly and all at once for a given cell. The breakdown appears to be triggered by a secondary vortex-ring-like flow structure which develops at the end of the first cell. Figure 6 is a multiple-exposure schlieren photograph and in this figure the internal vortex is indicated by an arrow. The origin and role of this feature appears to be as follows. The light fluid exiting the jet accelerates strongly, leading to a necking down of the flow at the end of the first cell. The shape of the cell and the degree of acceleration are determined by the condition that the streamwise pressure drop in the light fluid must match the pressure drop imposed by the hydrodynamic head in the heavier free stream. At the end of the first cell the interface between the fast-moving jet fluid and the slower co-flow is a region of high shear and is unstable owing to the high local Reynolds number. The buoyancy-generated vortex sheet rolls up to form the secondary vortex ring which accelerates rapidly upward with the core fluid. The downstream boundary of the cell is inclined to the direction of flow, creating an interface which is unstable in the Rayleigh–Taylor sense. High-speed movies of the flow show that breakdown of the cells follows shortly after the formation of the internal vortex ring. The surprising feature is that fine details of the breakdown process tend to be precisely repeated from cycle to cycle.

The adiabatic flame temperature of most hydrocarbon fuels burning in ambient air

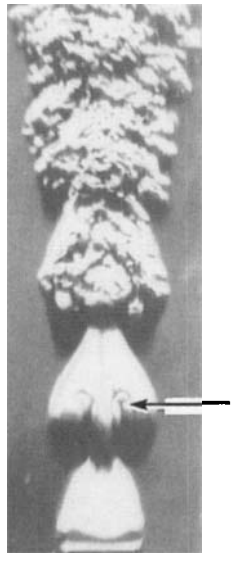

FIGURE 6. Typical photograph at $Re = 790$, $Ri = 1.6$. Arrow indicates a newly formed a vortex ring inside the second cell.

at 300 K is approximately 2100 K. Using these values and the exit flow parameters of the helium jet, the Richardson number of a flame is approximately $Ri = 1.5/U^2$ which is comparable to equation (4). So at least on the basis of density ratio a helium jet might be expected to behave hydrodynamically like a flame. There are also strong visual similarities (cf. figure 7 in Strawa & Cantwell 1989). Moreover the breakdown to turbulence through a Rayleigh–Taylor type of instability probably also plays a significant role in the flame. There are, however, fundamental differences between the two flows and these are seen most clearly in their contrasting response to forcing. While the structure of the helium jet is quite difficult to modify without large-amplitude forcing, the diffusion flame is extremely sensitive to small perturbations of the jet exit velocity. The high degree of sensitivity of the flame appears to be related to the manner in which buoyancy is released at the jet exit in the form of a cylindrical plume with its own inherent stability properties. The repeatability exhibited by the co-flowing helium jet is more dramatic than in the flame and occurs in the absence of forcing. Details of the stroboscopic schlieren image of the self-excited jet remain stationary over the span of several thousand cycles.

Figures 7 and 8 show four cases of Reynolds number and Richardson number for the weakly excited jet, chosen to permit comparison of the effect of Ri at constant Re for two values of Re and the effect of Re at constant Ri for two values of Ri. The combination of figures 5, 7 and 8 provides a view of the flow structure over most of the range of our experiments. Figures 7 and 8 each consist of two sets of four pictures. In each set the left-most photograph is a sixteen-shot multiple exposure and the three right-hand photographs are single-shot photographs taken several thousand cycles apart. The outline of the first few cells in the multiple exposure photographs is not blurred, indicating the streamwise extent over which the flow is accurately synchronized with the strobed light source. For the two cases in figure 7 at $Ri = 1.6$, the large-scale and even the fine-scale structures are highly repeatable. At $Ri = 1.6$, $Re = 390$ it is quite difficult to distinguish the multiple-exposure picture from the

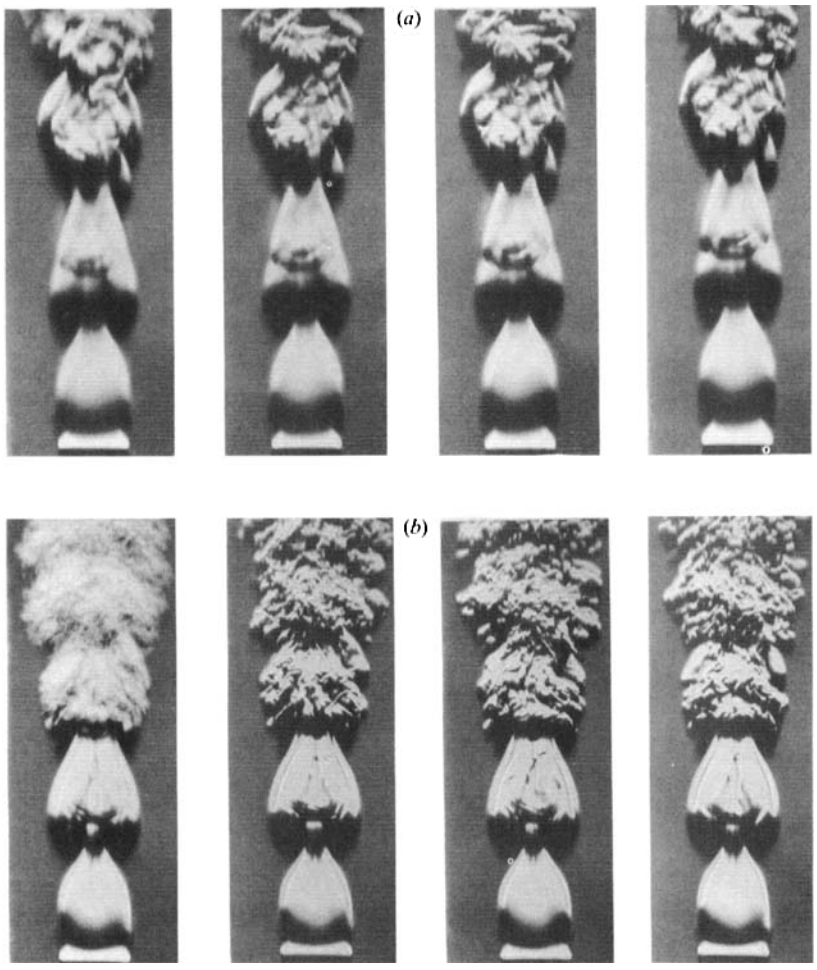

FIGURE 7. Schlieren photographs at $Ri = 1.6$ and (*a*) $Re = 390$; (*b*) $Re = 790$. The left-most photograph is multiply exposed 16 times. The three photographs on the right are single exposures taken several thousand cycles apart.

three right-hand photographs, indicating the precise long-term repeatability of the flow. At $Ri = 1.6$, $Re = 790$ blurring of the flow in the post-breakdown region is apparent in the multiple-exposure case; however, even in this case some detail of the fine structure can still be seen. At a Richardson number of 0.56 shown in figure 8 the fine scales are considerably less repeatable and increased blurring in the post-breakdown region is seen. Nevertheless the effects of buoyancy are still significant and in the highest Reynolds number case (figure 8*b*; $Ri = 0.56$, $Re = 1185$; Re based on air equals 8295) the first five wavelengths of the basic longitudinal instability are seen to repeat themselves quite clearly to a streamwise position of about three diameters.

Figures 7 (*a*) and 7 (*b*) depict a flow at moderate Reynolds number where the three-dimensional structure of the flow is organized and repeatable from cycle to cycle. The reasons for this behaviour are not understood but any explanation needs to take account of the fact that the Reynolds number based upon air properties is eight times greater than that based upon helium. Perturbations in the air stream are therefore

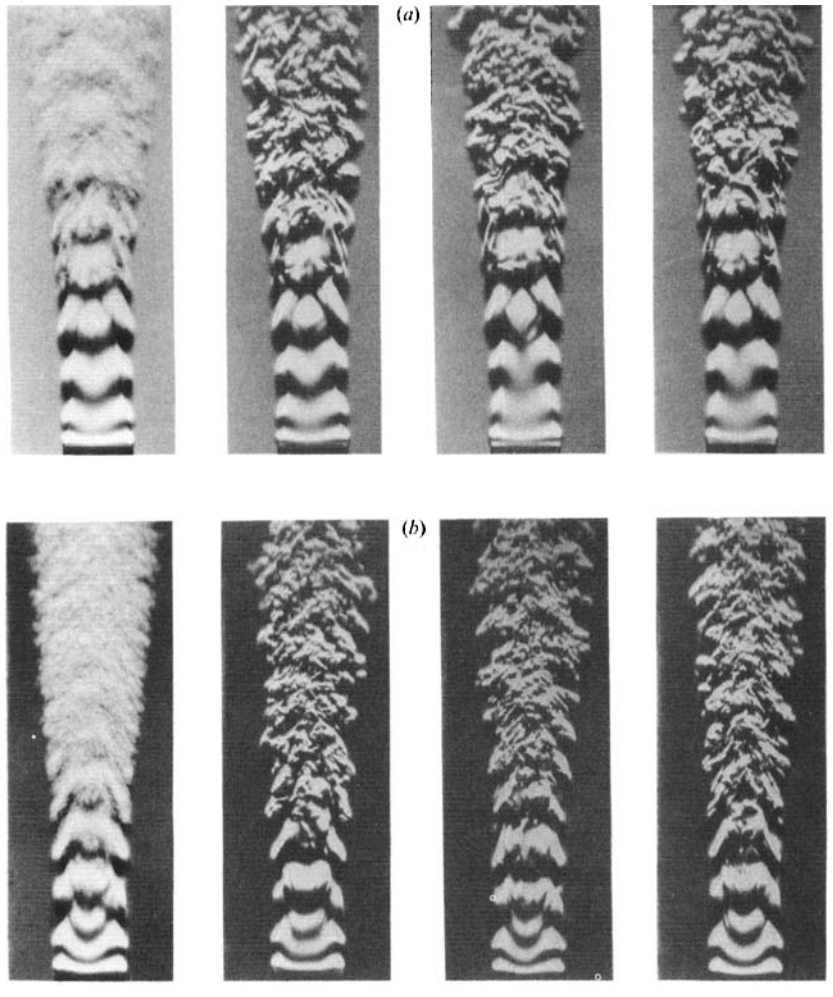

FIGURE 8. Schlieren photographs at $Ri = 0.56$ and (a) $Re = 790$; (b) $Re = 1185$. Exposures as for figure 7.

likely to have greater influence than in the helium stream and are likely to dominate transition. If disturbances exist in the surface boundary layer on the outside of the jet tube or in the free stream they will be convected into the jet and imprinted on the periodically forming cells of helium. Since interactions between adjacent cells in the near field are relatively weak with no tendency toward pairing or tearing evident in the visual data, the cells evolve primarily under the influence of co-flow stream disturbances without significant distortion by mutual straining. During the formation of the internal vortex depicted in figure 6, filaments of air are entrained into the cell and brought close to the centreline where the highest fluid velocities are found. Kelvin–Helmholtz instability of the vortex sheet leading to the formation of the internal vortex, Rayleigh–Taylor instability of the interface and the influence of free-stream disturbances all contribute to cell breakdown and probably all play a role in the repeatability of the three-dimensional structure.

4.2. *Natural-frequency behaviour*

The Richardson number can be interpreted as the ratio of two timescales. If we take $\tau_1 = D/U_j$ to be a measure of the time for a fluid element to move one jet diameter

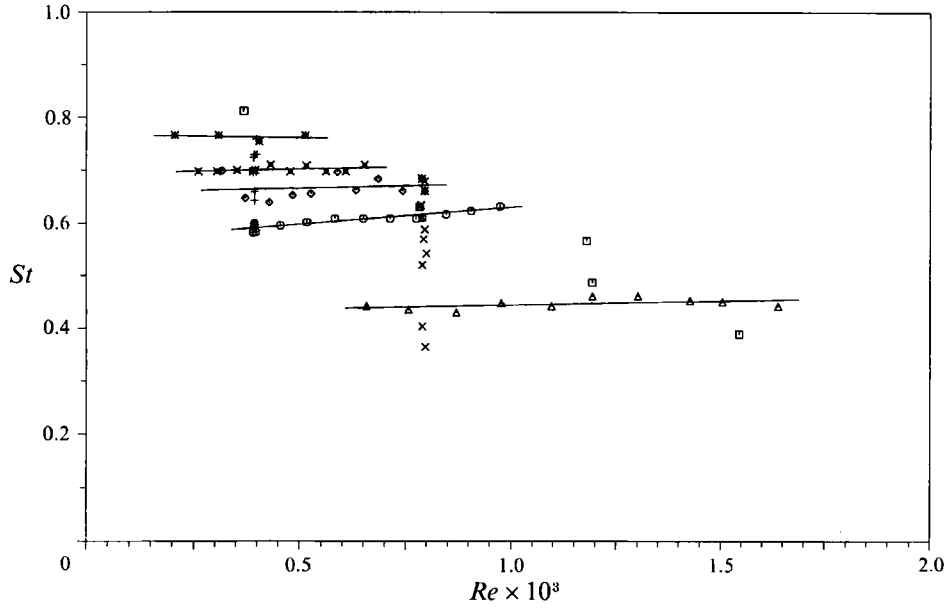

FIGURE 9. Strouhal number versus Reynolds number for the cases studied: +, $Re = 400$; ×, $Re = 800$; □, miscellaneous; △, $Ri = 0.57$; ○, $Ri = 1.6$; ◇, $Ri = 2.37$; ⊠, $Ri = 3.55$; *, $Ri = 5.68$.

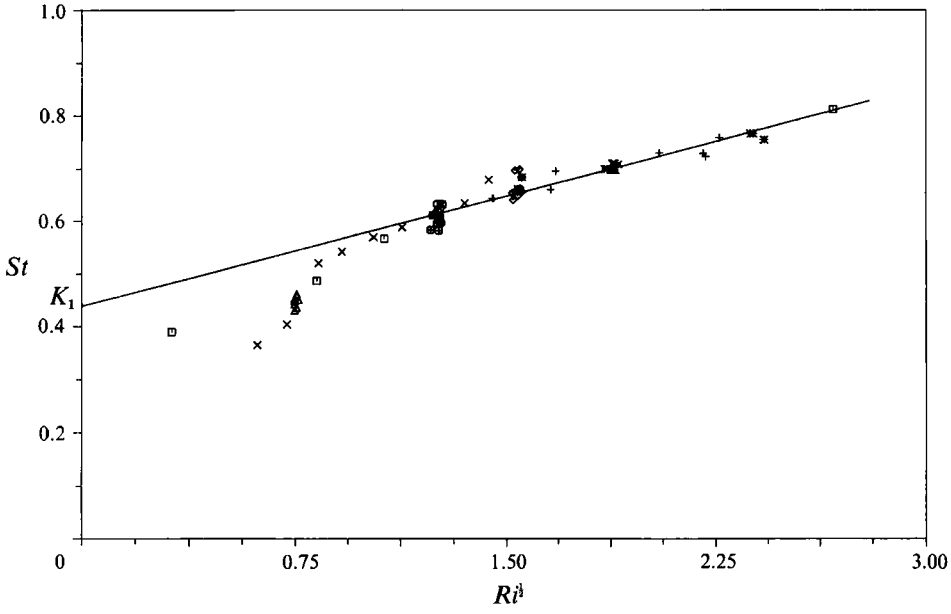

FIGURE 10. Strouhal number versus the square root of Richardson number. Symbols as figure 9.

under the action of inertia and $\tau_2 = [\rho_j D/g(\rho_\infty - \rho_j)]^{\frac{1}{2}}$ to be a measure of the time for a fluid element to move one jet diameter under the action of buoyancy then

$$Ri = (\tau_1/\tau_2)^2. \tag{6}$$

The Strouhal number St is traditionally defined using the inertial timescale

$$St = fD/U_j. \tag{7}$$

Figure 9 shows the Strouhal number plotted versus the Reynolds number for various

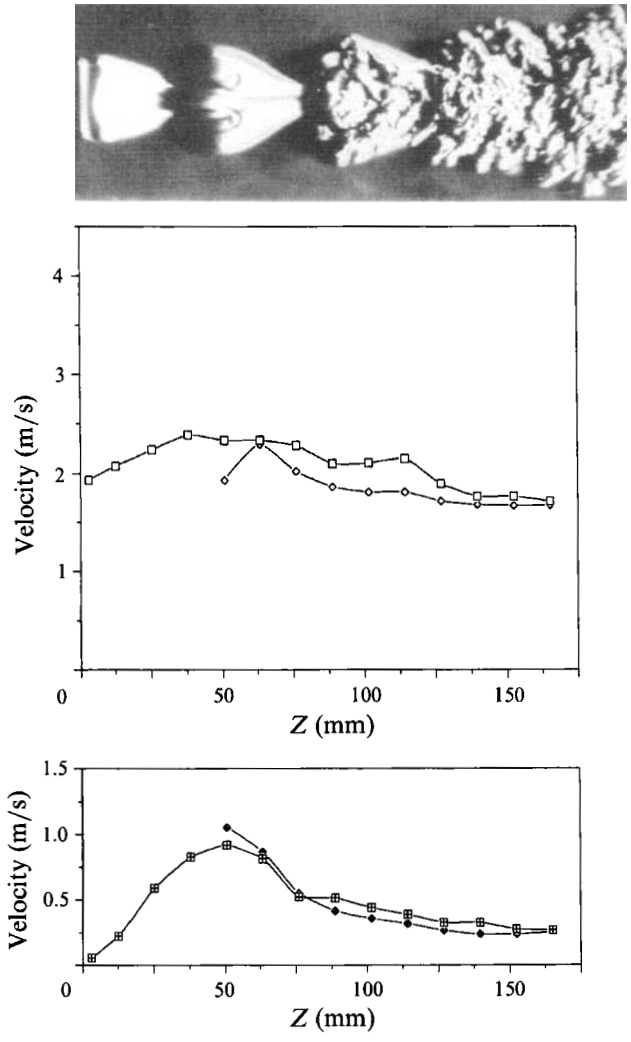

FIGURE 11. Axial distribution of mean streamwise velocity measured with inner- and outer-flow seeding at $Re = 790$, $Ri = 1.6$. The accompanying photograph is included for reference purposes. Inner: □, $\bar{U}$; ⊞, $U_{\rm rms}$. Outer; ◇, $\bar{U}$; ⊕, $U_{\rm rms}$.

Richardson numbers. It is clear that over the range of the experiments the Strouhal number is nearly independent of the Reynolds number, and any variation with Reynolds number collapses within the limits of scatter, but is strongly dependent on the Richardson number. Figure 10 shows a plot of the Strouhal number versus the square root of the Richardson number. For Richardson numbers greater than unity, the data for all Reynolds numbers fall on a straight line. For Richardson numbers below a critical value of 0.51 the Strouhal number is approximately constant and equal to 0.4. The transition from inertially to buoyancy-dominated flow occurs over a narrow range of Richardson numbers between 0.5 and 1.0. The strong dependence of St on Ri suggests that the flow natural frequency ought to be normalized by the buoyancy timescale. We define a buoyancy Strouhal number

$$St = \frac{(fD/U_j) - K_1}{Ri^{\frac{1}{2}}}, \tag{8}$$

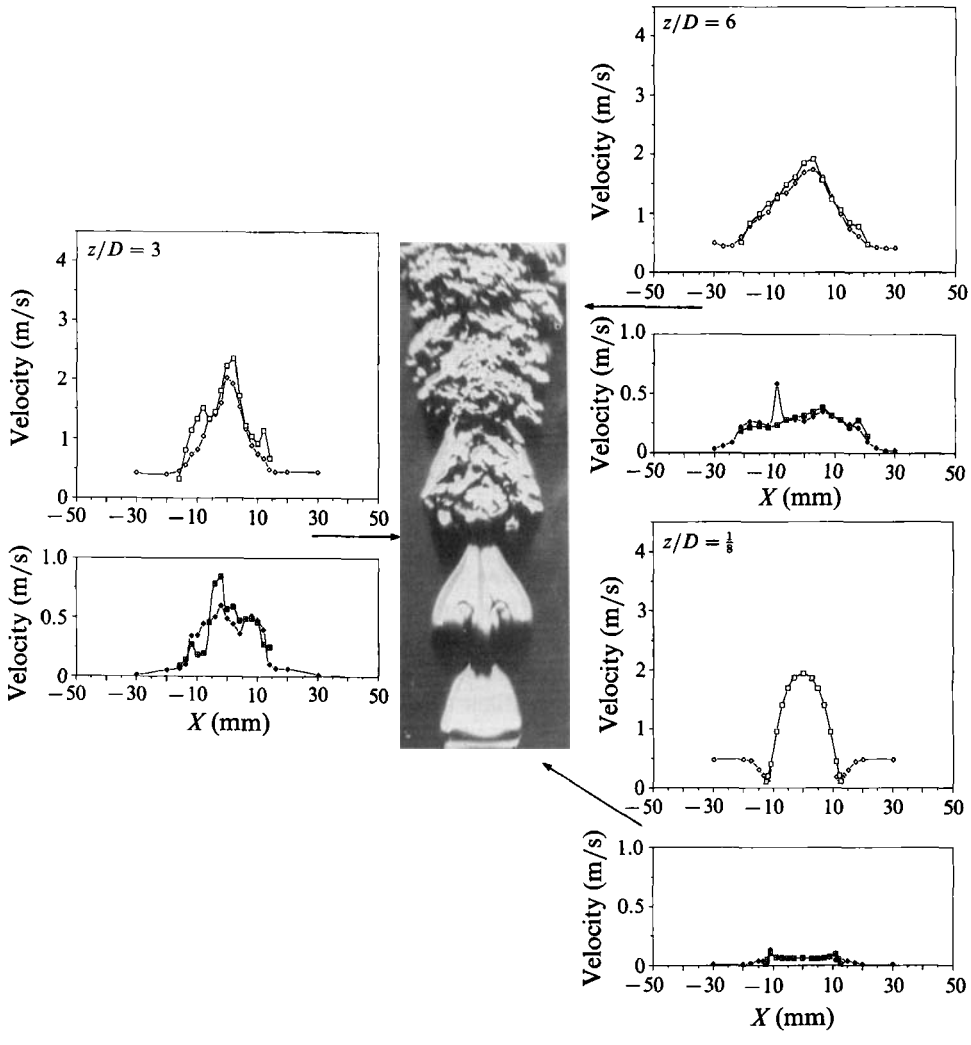

FIGURE 12. Radial distribution of mean streamwise velocity at three stations measured with inner-and outer-flow seeding at $Re = 790$, $Ri = 1.6$. Symbols as figure 11.

where K_1 is emperically chosen as 0.445 for these data. The buoyancy Strouhal number, for Richardson number greater than one, is approximately constant at the value 0.136.

4.3. *Mean flow behaviour*

In §4.1 we discussed the rather unusual unsteady structure of this flow; we now turn to a discussion of the average properties of the flow. A more typical ordering would generally consider the mean motion first before proceeding to the complexities of the unsteady flow which underlies it. However, there are features of the mean flow field which can only be understood in terms of the instantaneous picture. Figure 11 is a plot of the long-time mean velocity and root-mean-square velocity fluctuation at several stations along the jet centreline. An instantaneous schlieren photograph of the flow is included for reference to help delineate various flow zones evident in the mean profile. It should be noted that the measurements in figure 11 correspond to a situation where either the inner or outer fluid is seeded. In the case of inner flow

seeding the velocity should be understood to correspond to a global mean that is conditioned, not on helium which diffuses beyond the seed particles into the surrounding air, but on an undiffused, sharply bounded image of the jet fluid. Buoyancy-induced acceleration of the mean velocity occurs only in the first 1.5 diameters after which the centreline flow decelerates through mixing. The decaying portion of the velocity distribution is not smooth but contains several bumps. The mean velocity with outer-flow seeding is close to but consistently below the mean velocity of the jet fluid, indicating a significant degree of 'unmixedness' with respect to the mixing of momentum. Fluctuation levels build up sharply for the first 2 diameters and then drop off to a gently decaying curve beyond 3 diameters. As with the mean, the fluctuations of the outer fluid are below those of the jet fluid except between 2 and 3 diameters where the two are nearly matched.

Jaggedness in the mean profiles is also evident in figure 12 which depicts three transverse velocity profiles measured at the three downstream stations indicated in figure 1. As in figure 11 an instantaneous photograph is included for reference. Mean velocity profiles for both inner- and outer-flow seeding are included in figure 12. At the jet exit the mean velocity profile is smooth and close to parabolic. The wake of the jet tube is apparent and the boundary layer on the outside of the jet tube is close to a Blasius shape. At $Z/D = 3$ mixing has taken place with a considerable amount of jet fluid reaching the centreline. Both mean velocity profiles have taken on a strongly peaked shape and, although the profiles are somewhat similar, the inner fluid profile has two well-defined peaks on either side of the centerline. By $Z/D = 6$ the peaks have mixed out and the two profiles are nearly the same. At this point the competition between buoyancy, which tends to speed up the jet fluid, and mixing, which tends to homogenize the jet and free-stream fluid, is being won by mixing. The rather sharply peaked shape of the profile at $Z/D = 6$ seems to be characteristic of this class of buoyant flows and also shows up in the flame data of Strawa & Cantwell (1989). The difference between the inner seeded profile and the outer seeded profile is particularly clear three diameters downstream of the jet exit. The peak velocity of the outer seeded profile is lower than that of the inner seeded flow. The outer seeded profile is also narrower than that with inner seeding. These differences are consistent with the mechanism by which outer seed particles are brought within the jet boundary. The outer seed is carried by the co-flow fluid which is slower than the jet fluid. Within the boundaries of the jet, outer seeded fluid is found as slower moving intrusions. The mean velocity near the centreline, measured with the outer flow seeded should therefore be lower than that measured with inner seeding. Away from the centreline there is more mixing of the outer co-flow fluid with the jet fluid and the effect of the slower co-flow fluid on the velocity measurements is more pronounced, leading to a narrower profile.

The spiky nature of the mean data, particularly the profiles at $Z/D = 3$, can be explained by returning to the photographs in figure 7(*b*) which illustrated the repeatability of the unsteady flow structure and can help us understand the nature of the repeatability. In the transition region between $Z/D = 1$ and 3 there apparently exist deep intrusions of heavy fluid some of which, at certain phases of the cycle, may reach the flow centreline. The light fluid rises in this convecting array of low-speed intrusions and one can conjecture that if a parcel of light fluid establishes a particular path then this may become a path of least resistance for parcels which follow. Such a path might become 'locked in'. accounting for the repeatability and the tendency for some of the detailed structure to persist even when a long-time average is formed.

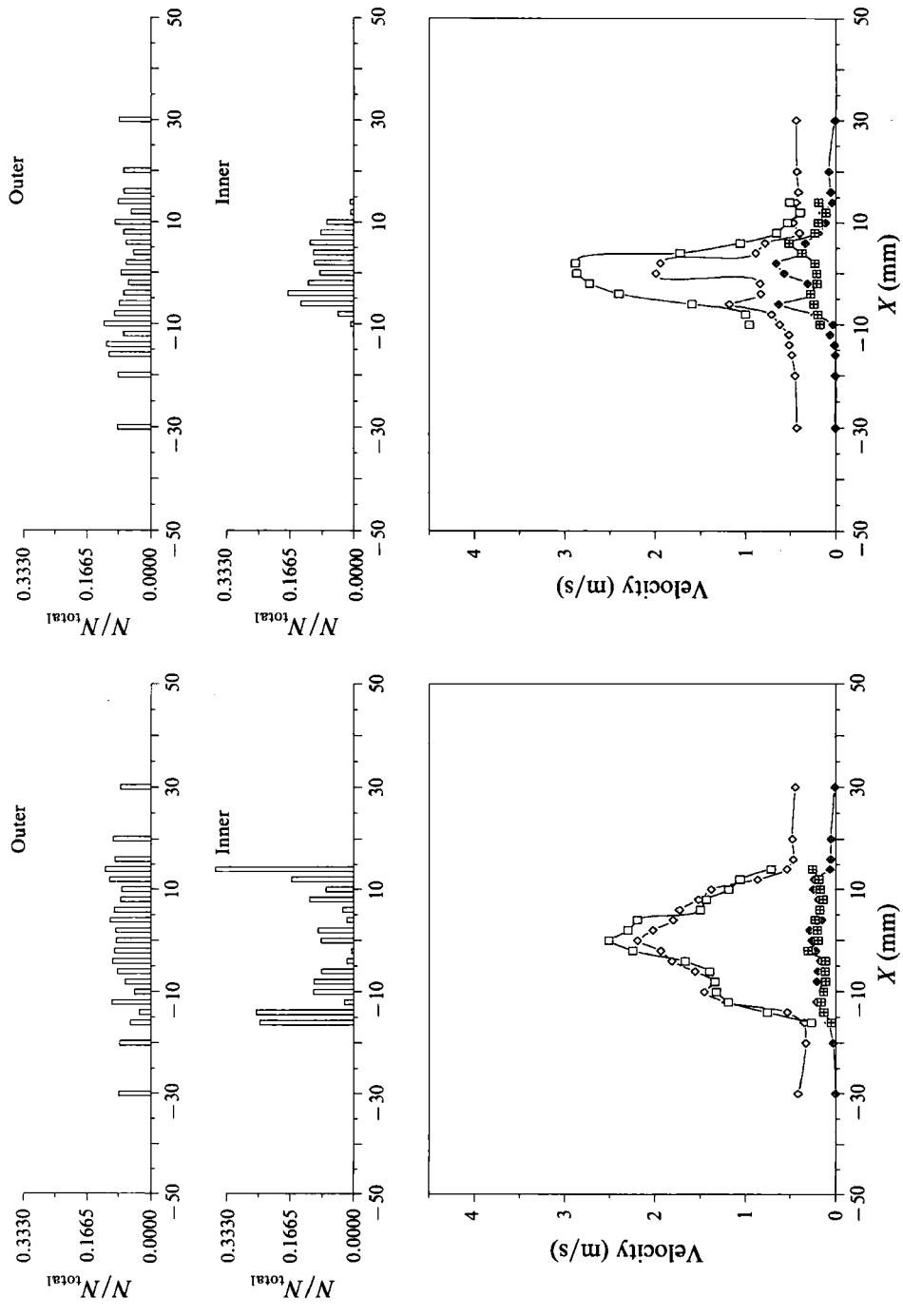

FIGURE 13. Radial distribution of ensemble-averaged velocity at two phase intervals including population density histograms with inner- and outer-flow seeding at $Re = 790$, $Ri - 1.6$, $Z/D = 3$. Symbols as figure 11.

4.4. *Variation within a cycle*

Figure 13 shows velocity profiles across the jet for inner- and outer-flow seeding at 3 diameters from the jet exit. In these figures the data are averaged at constant phase for two typical 30° phase intervals half a cycle apart. The profiles are for the same case as depicted in figure 12 (Case C, $Re = 790$, $Ri = 1.6$, $Z/D = 3$). The streamwise velocity profiles are a strong function of phase. Spikes of the kind observed in the global mean velocity profiles occur with even larger amplitude and steeper velocity gradients than in the average at constant phase. At a given radial location and phase the velocity of the outer fluid is, again, consistently lower than that of the inner fluid. Included above each plot are the histograms of population densities at each measurement point across the jet for inner- and outer-flow seeding. These are the fraction of data points that lie within the phase interval collected at each location. Comparison of the population histograms for inner seeding at the two phase intervals reveal some interesting features. In one case, at about 5 mm left of the centreline, there is a gap in the inner seed, whereas there is a significant population of outer seed samples. During the other phase interval at the same location, there is clearly no gap in either the inner seed or the outer seed. A check of all phase intervals reveals that, at this streamwise station ($Z/D = 3$), gaps in outer flow seeding do not occur within the boundaries of the jet whereas gaps in the inner fluid are relatively common. This provides further support for the presence of low-speed intrusions of heavy fluid discussed at the end of the last section, but also indicates that there is significant variation of the flow within the 30° phase interval of the phase averages.

4.5. *Velocity ensembles on the centreline*

As noted in the discussion of figure 13, at a given point during a given phase interval, there are usually significant numbers of both inner- and outer-fluid samples recorded. This is partly because the repeatability of the fine structure of the flow is not perfect; there is some cycle-to-cycle jitter. It is also a reflection of the fact that the phase intervals are of finite width and therefore flow features which may deserve to be separated are lumped together. To study the structure of the velocity field without the smoothing that is caused by averaging over a 30° phase interval, complete data ensembles are plotted in figure 14 (Case B, $Re = 790$, $Ri = 1.6$) and figure 15 (Case C, $Re = 390$, $Ri = 1.6$). Although the following discussion will be devoted to the higher Reynolds number, the reader may wish to refer to figure 15 for comparison and for confirmation that the features discussed occur at both Reynolds numbers. Note that the data presented in figures 14 and 15 are for a situation where only the jet fluid is seeded and that downstream of $Z/D = 2$ free-stream fluid can reach the centreline. At each spatial location 2800 velocity data points were collected along with the associated phase of the flow excitation signal. In figure 14 all data points for the case of inner-flow seeding are plotted as a function of phase at each of eight streamwise locations along the jet centreline. These plots show the streamwise development and breakdown of the periodic waveform associated with acceleration of the jet fluid and transition to turbulence. Just downstream of the jet exit ($Z/D = \frac{1}{8}$) the flow shows a small-amplitude periodic oscillation. At $Z/D = 6$ the velocity measurements have assumed a shape which might be expected in a fully mixed turbulent jet with little variation with phase. This is consistent with the behaviour suggested by the schlieren photographs of this case shown in figure 7(*b*). The stations between $Z/D = \frac{1}{8}$ and 6 depict a complicated, highly structured, process of transition and breakdown to turbulence.

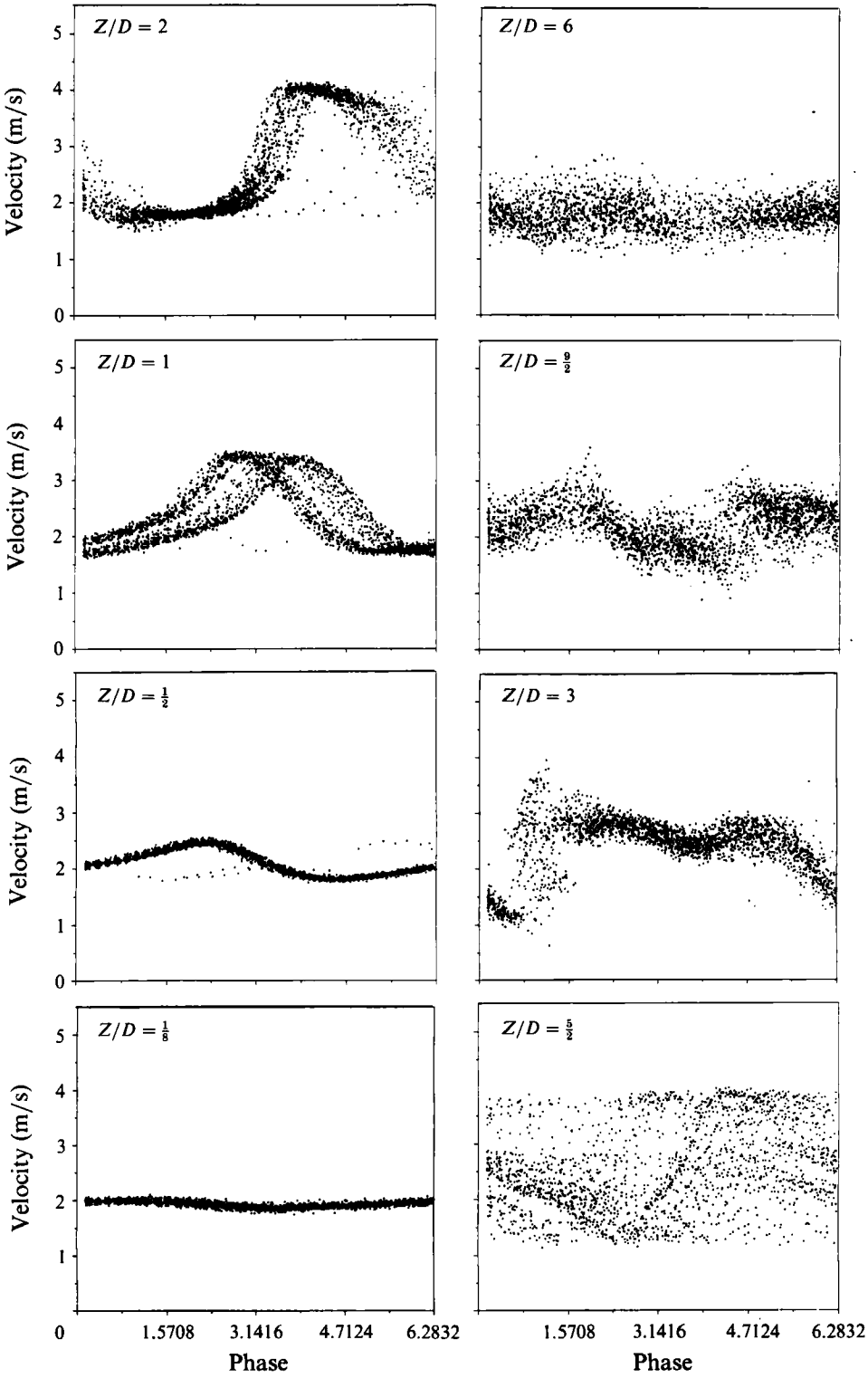

FIGURE 14. Velocity versus phase at several axial stations ($Re = 790$, $Ri = 1.6$).

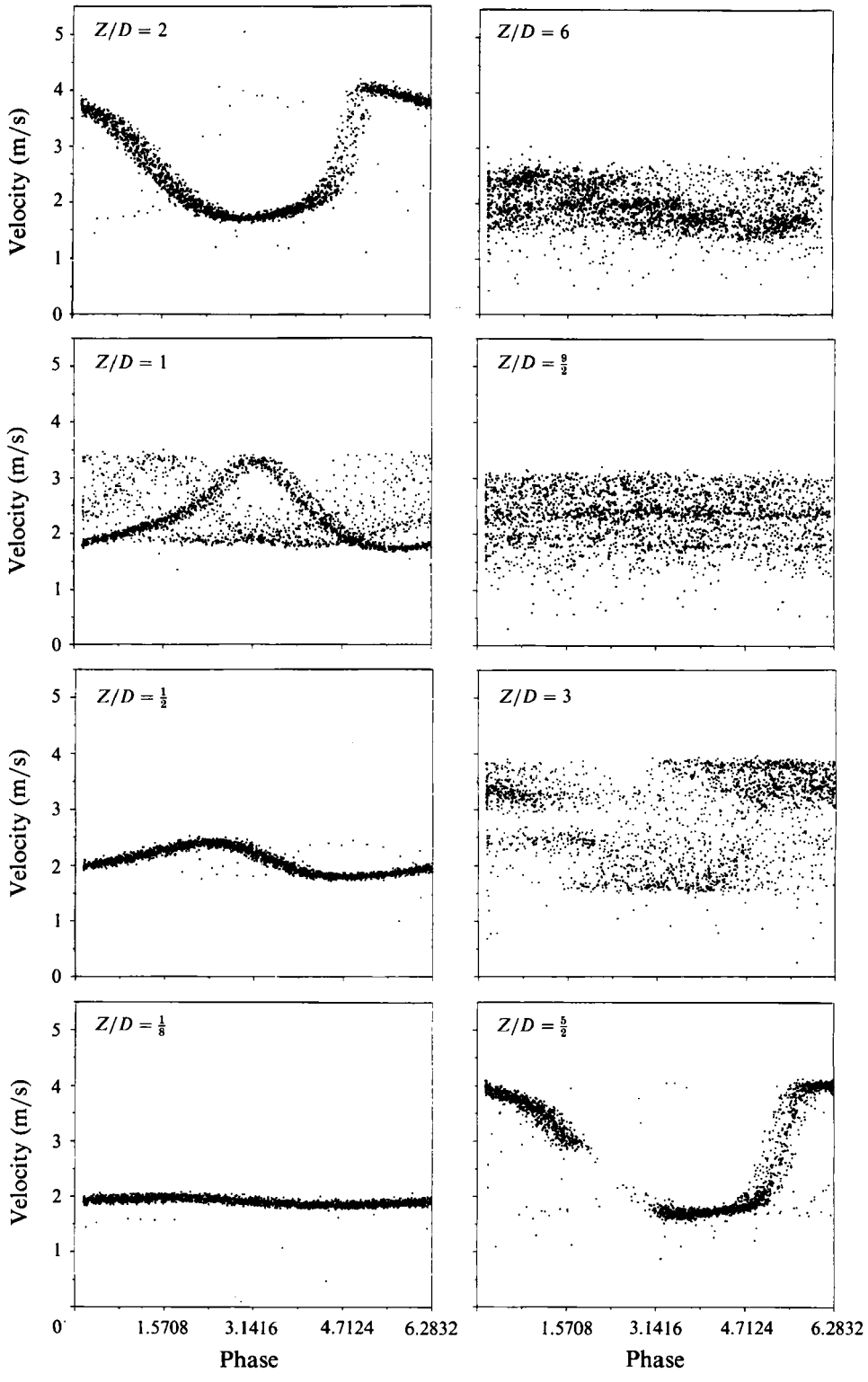

FIGURE 15. Velocity versus phase at several axial stations ($Re = 390$, $Ri = 1.6$).

Referring to figure 11 we see that the measurements at $Z/D = \frac{1}{8}$, $\frac{1}{2}$ and 1 are characterized by the fact that only jet fluid is encountered and the velocity variation is sinusoidal. At $Z/D = \frac{1}{2}$ the amplitude of the velocity fluctuations has grown appreciably and a slightly nonlinear, repeatable, waveform is established. At $Z/D = 1$ the waveform is seen to split into two clearly defined modes. Both modes have approximately the same shape, but are displaced in phase with respect to each other. Figure 15 at the lower Reynolds number shows a similar splitting at $Z/D = 1$ except that the trace breaks up into several identifiable clusters. The data at $Z/D = 1$ show that the flow is not perfectly repeatable, nor is it random in the usual sense; but can jump between two or more states of motion. The character of the data at $Z/D = 1$ may be explained as follows. With strong buoyancy, the parabolic exit profile will rather rapidly develop a strong peak on the centreline. On the basis of the previous discussion, this peak may define the location of a preferred pathway for light fluid rising through the surrounding heavy fluid. If, along with the longitudinal oscillations, there exists any tendency for the preferred path to shift position then large velocity changes will result. The same shift in position would produce relatively small velocity changes at the jet exit. The shifting of the preferred path may occur continuously in the form of spiralling or wobbling of the peak in the velocity profile or it may occur in discrete jumps over a period that is long compared to the basic oscillation period. The latter description is suggested by laboratory observations of the schlerien image.

At $Z/D = 2$ and 3 traces of the waveforms can still be seen. The presence of clusters where the data tend to collect is evidence that the changes in flow state that do take place are repeatable. It is possible that the same patch switching suggested to explain the curves at $Z/D = 1$ can also explain the form of the data at $Z/D = \frac{5}{2}$ except that the velocity profile is now much more complicated. Increased mixing is evident in the curves at $Z/D = 3$ and $\frac{9}{2}$ although the basic buoyancy-driven periodicity of the flow is still clearly evident. The data in figure 15 are qualitatively similar to those in figure 14 except that clusters of data are perhaps more clearly seen and persist to larger values of Z/D, as one might expect in view of the reduced Reynolds number. At $Z/D = \frac{5}{2}$ in figure 15 a break in the data can be seen, associated with pinching-off of the centreline flow by entrained air.

5. Conclusions

The flow studied here is representative of a broad class of low-speed variable-density jets which arise in practical applications. It is clear from the results of this and an earlier study on flames that, in a range of Richardson numbers somewhat above unity, this class of flows is subject to an unusual type of transition to turbulence consisting of a rapid but highly structured and repeatable breakdown and intermingling of jet and free-stream fluid. Comparisons of the controllability and natural-frequency dependence of both the helium jet and the flame lead to the conclusion that the spatial distribution of buoyancy released near the origin of the flow plays an important role in determining the downstream development of this class of flows. In the helium jet buoyancy is released approximately uniformly across the jet exit and, for Richardson numbers greater than one, the natural frequency of the flow is well correlated by a buoyancy Strouhal number.

This work has been supported in part by NASA grants NCC 2-21 and NAG 2-382 and by the Office of Naval Research under grant N00014-90-J-1976-P00001.

REFERENCES

BALLANTYNE, A. & BRAY, K. N. C. 1977 Investigations into the structure of jet diffusion flames using time-resolved optical measurement techniques. In *Sixteenth (Intl) Symp. on Combustion*, pp. 777–787. The Combustion Institute.

BECKER, H. A. & LIANG, D. 1983 Soot emission, thermal radiation and laminar instabilities of acetylene diffusion flames. *Combust. Flame* **52**, 247–256.

CHAMBERLIN, D. S. & ROSE, A. 1928 The flicker of luminous flames. *Ind. Engng Chem.* **20**, 1013–1016.

CHEN, C. J. & RODI, W. 1980 *Vertical Turbulent Buoyant Jets: A review of Experimental Data.* Permagon.

FAY, J. A. 1973 Buoyant plumes and wakes. *Ann. Rev. Fluid Mech.* **5**, 151–161.

GEBHART, B., HILDER, D. S. & KELLEHER, M. 1984 The diffusion of turbulent buoyant jets. *Adv. Heat Transfer* **16**, 1–57.

GRANT, A. J. & JONES, J. M. 1975 Low frequency diffusion flame oscillations. *Combust. Flame* **25**, 153–160.

KIMURA, I. 1965 Stability of laminar jet flames. In *Tenth (Intl) Symp. on Combustion*, pp. 1295–1300. The Combustion Institute.

SCHONBUCHER, A., ARNOLD, B., BANHARDT, V., BIELLER, V., KASPER, H., KAUFMANN, M., LUCAS, R. & SCHIESS, N. 1986 Simultaneous observation of organized density structures and the visible field in pool fires. In *Twenty-first (Intl) Symp. on Combustion*, pp. 83–92. The Combustion Institute.

STRAWA, A. W. 1986 An experimental investigation of the structure of an acoustically excited diffusion flame. Ph.D. thesis, Stanford University, Department of Aeronautics and Astronautics.

STRAWA, A. W. & CANTWELL, B. J. 1989 Investigation of an excited jet diffusion flame at elevated pressure. *J. Fluid Mech.* **200**, 309–336.

SUBBARAO, E. R. 1987 An experimental investigation of the effects of Reynolds number and Richardson number on the structure of a co-flowing buoyant jet, *SUDAAR* 563. Stanford University, Department of Aeronautics and Astronautics.

ZUKOSKI, E. E., CETEGEN, B. M. & KUBOTA, T. 1984 Visible structure of buoyant diffusion flames. In *Twentieth (Intl) Symp. on Combustion*, pp. 361–366. The Combustion Institute.